

Cite this: *Catal. Sci. Technol.*, 2018,  
8, 6503

## Efficient light-driven CO<sub>2</sub> hydrogenation on Ru/CeO<sub>2</sub> catalysts†

Fengjiao Quan,<sup>a</sup> Guangming Zhan,<sup>a</sup> Chengliang Mao,<sup>a</sup> Zhihui Ai,<sup>a</sup> Falong Jia, \*<sup>a</sup>  
Lizhi Zhang, <sup>a</sup> Honggang Gu<sup>b</sup> and Shiyuan Liu <sup>b</sup>

Light-driven heterogeneous catalysis provides a promising way to accomplish chemical reactions by the use of light energy, which reduces the consumption of chemical energy sources. Here, we show that Ru/CeO<sub>2</sub> catalysts exhibit high activity for the hydrogenation of CO<sub>2</sub> to methane under illumination only, reaching high CO<sub>2</sub> conversion (over 99.9%) and selectivity of methane (~100%) at low temperature. In sharp contrast, less CO<sub>2</sub> is converted at the same temperature when a traditional heating model is used. As revealed by the results, the enhanced conversion rate under illumination should not only be attributed to the light-induced thermo-heating. Further investigations by *in situ* IR analysis and theoretical calculation provide comprehensive understanding of the reaction mechanism, and the important role of light is revealed. It is expected that the combination of catalysts and light may afford new perspectives for CO<sub>2</sub> hydrogenation.

Received 26th August 2018,  
Accepted 11th November 2018

DOI: 10.1039/c8cy01787e

rsc.li/catalysis

### 1. Introduction

The capture and utilization of CO<sub>2</sub> is of great importance for the reduction of CO<sub>2</sub> emission, which would contribute to the alleviation of global climate changes. Moreover, CO<sub>2</sub> could be used as an attractive C1 building block for production of valuable chemicals through the hydrogenation route.<sup>1–6</sup> Nowadays, effective CO<sub>2</sub> hydrogenation is still challenging due to the difficulties in the activation of thermodynamically stable CO<sub>2</sub>. As a result, conventional thermal-catalytic CO<sub>2</sub> hydrogenation has to be operated at a relatively high temperature to obtain a satisfactory conversion rate. In this process, the consumption of thermal energy may also bring extra CO<sub>2</sub> emissions. From the aspect of green CO<sub>2</sub> recycling, it is desirable that a renewable energy (*e.g.* solar light) could be used to drive CO<sub>2</sub> conversion.

Recently, a photothermal strategy is proposed for the light-driven CO<sub>2</sub> hydrogenation and other reactions over various catalysts.<sup>7–10</sup> These experimental results indicate that the solar-light induced photothermal effect dominates the process of CO<sub>2</sub> conversion. This technique provides a promising route for the utilization of solar light in the CO<sub>2</sub> conversion.

Before the application of this technology in large-scale industrial production, there are still some challenges that need to be addressed. One key challenge is the development of efficient catalysts suitable for this special illumination process. At present, the working temperature for CO<sub>2</sub> hydrogenation is relatively high. It is of great importance to reduce the hydrogenation temperature for efficient utilization of solar light.

Based on the present mechanisms for the thermal CO<sub>2</sub> hydrogenation over metal nanoparticles/oxide catalysts, metal-oxide support can significantly influence the activity of the catalysts.<sup>11</sup> As one of the promising oxide supports toward CO<sub>2</sub> conversion, CeO<sub>2</sub> has attracted wide interest due to its unique structural features resulting from its reversible valence change.<sup>12</sup> In particular, the CeO<sub>2</sub> materials facilitate the CO<sub>2</sub> adsorption and promote the CO<sub>2</sub> conversion rate through the activation of the carbon–oxygen bond during the thermocatalytic process.<sup>13,14</sup> As for the light-involving CO<sub>2</sub> hydrogenation process, the detailed roles of the light and catalytic mechanism of the catalyst remain unclear, which need to be studied to provide instructions for the development of robust catalysts. Moreover, the adsorption and transformation of intermediate species on the catalyst may be affected by photo-irradiation, whereas this has been scarcely discussed in light-driven CO<sub>2</sub> methanation.

Herein, we report an efficient light-driven CO<sub>2</sub> methanation system that employs a thin-layer flow cell loaded with a model Ru/CeO<sub>2</sub> catalyst. Both high conversion of CO<sub>2</sub> to methane (99.9%) and selectivity (~100%) are achieved under an illumination of 1.1 W cm<sup>-2</sup>. *In situ* FTIR measurements were utilized to study the effect of light on the CO<sub>2</sub>

<sup>a</sup> Key Laboratory of Pesticide & Chemical Biology of Ministry of Education, Institute of Environmental Chemistry, College of Chemistry, Central China Normal University, Wuhan 430079, P. R. China. E-mail: fljia@mail.ccnu.edu.cn

<sup>b</sup> State Key Laboratory of Digital Manufacturing Equipment and Technology, Huazhong University of Science and Technology, Wuhan 430074, P. R. China

† Electronic supplementary information (ESI) available. See DOI: 10.1039/c8cy01787e

hydrogenation. It is hoped that this investigation would provide solution for the design and synthesis of efficient catalysts for solar-driven CO<sub>2</sub> transformation.

## 2. Experimental

### 2.1 Preparation of the Ru/CeO<sub>2</sub> catalyst

The CeO<sub>2</sub> catalyst was synthesized by a microwave-assisted nonaqueous sol-gel method with reference to a previous report.<sup>15</sup> In a typical synthesis, 5 mmol Ce(III) acetylacetonate (Aldrich) and 30 mL benzyl alcohol (Aldrich) were added into a 50 mL flask equipped with a condenser pipe. This flask was then placed in a microwave oven (MAS-1, 2.45 GHz, Shanghai Xinyi Ltd.) and heated to 200 °C under magnetic stirring. After 30 min of continuous reflux at 200 °C, the precipitate was separated from the mixture by centrifugation and washed with ethanol. After that, the precipitate was calcined at 300 °C in an air atmosphere for 30 min and its color changed to light-yellow.

The Ru/CeO<sub>2</sub> catalyst with a Ru loading of 1.5 wt% was prepared by the following adsorption-decomposition method. First, 0.2 g CeO<sub>2</sub> powder was dispersed into 50 ml tetrahydrofuran solution containing 6.3 mg triruthenium dodecacarbonyl (Aldrich). This mixture was subjected to ultrasonic treatment (200 W) for 2 h at room temperature. After that, the tetrahydrofuran solvent was removed under vacuum and the powder was heated at 100 °C for 30 min in air. The resulting RuO<sub>2</sub>/CeO<sub>2</sub> sample was then reduced in a gaseous mixture of H<sub>2</sub> and Ar (1:9, v/v) for 1 h at 200 °C with a heating rate of 10 °C min<sup>-1</sup>. The obtained catalyst was denoted as Ru/CeO<sub>2</sub>.

### 2.2 Physical characterization of the catalyst

XRD was recorded on a Philips MPD 18801 diffraction-meter (CuK $\alpha$  radiation,  $\lambda = 1.5418$  Å, 20KV, 150 mA). The morphologies of the samples were observed using JEOL-6700F scanning electron microscopy (SEM). TEM and high resolution TEM analysis were performed by using JEM 2010FEF TEM operating at a voltage of 200 kV. Energy dispersive spectrometry (EDS) measurement was performed by using Oxford INCA. The diffuse reflectance UV-visible spectra of the samples were recorded on a spectrophotometer (UV-3600, Shimadzu, Japan) and BaSO<sub>4</sub> was used as a reflectance standard. X-ray photoelectron spectroscopy (XPS) was conducted using a Thermo Scientific K-Alpha XPS spectrometer with a monochromated X-ray source (aluminum K $\alpha$ ). The C 1s peak arising from adventitious hydrocarbons was assigned an energy value of 284.8 eV and used as an internal binding energy reference.

The reduction properties of the catalysts were measured using temperature-programmed reduction (TPR) techniques. A 100 mg sample was placed in a quartz reactor and degassed under flowing argon at 200 °C for 2 h. After cooling down to room temperature, a stream of H<sub>2</sub>/Ar (1:9, v/v) was introduced and the sample was heated to 900 °C at a heating rate of 20 °C min<sup>-1</sup>. The amount of H<sub>2</sub> consumption during the reduction was measured using a thermal conductivity detector (TCD).

### 2.3 Evaluation of catalytic performance

The CO<sub>2</sub> hydrogenation was carried out using a homemade quartz reactor at atmospheric pressure. The quartz flow cell has a rectangular structure with a size of 30 mm in length and 10 mm in width (Fig. S1†). The inner gap in the flow cell is 3 mm. 0.05 g catalyst powder was spread uniformly on the bottom of the cell with an interval of around 1 mm left for the gas flow. The temperature inside the reactor was measured using a thermocouple. Before CO<sub>2</sub> hydrogenation, the catalyst samples were reduced in a gaseous mixture (5% H<sub>2</sub> and 95% Ar in volume) for 1 h at 200 °C. After cooling down to room temperature, the reaction gas mixture (10% CO<sub>2</sub>, 42% H<sub>2</sub>, and 48% Ar in volume) was introduced into the reactor at a flow rate of 1 ml min<sup>-1</sup>. Under illumination, the flow cell reactor was irradiated using a 300 W Xe lamp (Beijing Perfectlight Technology, PLS-SXE300, filtered light,  $\lambda < 800$  nm). To evaluate the catalytic performance of the samples, we used three different reaction conditions (Fig. 1).

Under “illumination (a)”, the illumination power of the Xe lamp was adjusted to maintain the temperature of the catalyst inside the reactor. After the temperature was stabilized for at least 20 min during the gas flow, the gas products were analyzed using GC equipment. For the CO<sub>2</sub> hydrogenation under “heating (b)”, the flow cell is placed on a hotplate (IKA C-MAG HS7) to achieve the expected temperature. Under “illumination + heating (c)”, the illumination power was controlled to be a specified value, and assistant heating from the hotplate was applied to reach a target temperature of the catalyst. Corresponding images of the setup are presented in Fig. 2.

Gas products (CO and CH<sub>4</sub>) and remaining CO<sub>2</sub> were then injected into a gas chromatograph (GC-2020, Hengxin) equipped with a packed column (ZKAT-Z13 PLOT, ATEO) to realize the separation of CO<sub>2</sub> and products. These gases would flow through a nickel methanizer in which the unreacted CO<sub>2</sub> and CO were converted to detectable methane using a flame ionization detector. The following quantification was performed based on the correlation of the concentration of gases and corresponding peak areas.

### 2.4 IR analysis of the catalytic processes with a DRIFT device

*In situ* IR spectra were collected on a Nicolet IS50 (liquid N<sub>2</sub>-cooled MCT detector) instrument equipped with a DRIFT

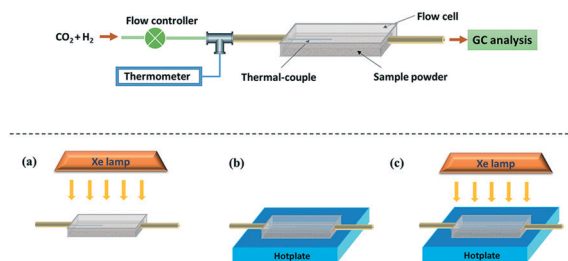


Fig. 1 Schematic illustration of the setup for the CO<sub>2</sub> hydrogenation (top) and three different reaction models (bottom): “illumination” (a), “heating” (b) and “illumination + heating” (c).

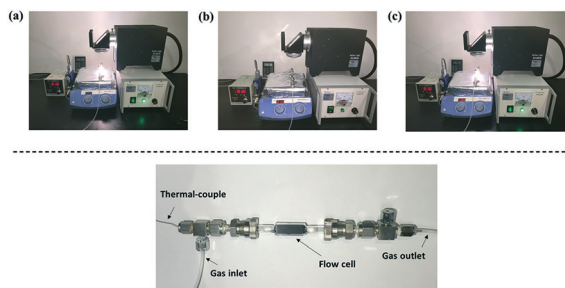


Fig. 2 (top) Images of the setup under three different reaction conditions: “illumination only (a)”, “heating only (b)” and “illumination + heating (c)”. (bottom) An image of the assembly of the flow cell.

accessory and a cell (Harrick). The spectra (the average of accumulated 32 scans) were recorded at a resolution of  $4\text{ cm}^{-1}$  with reference to adequate background spectra of the clean sample. The powder sample was pressed onto a tungsten mesh which was attached to the copper heating cup of the cell. The temperature of the sample was monitored using a thermocouple fixed on the top center of the tungsten mesh. To reveal the intermediates generated during the practical  $\text{CO}_2$  reduction, the IR measurements were carried out at atmospheric pressure and the cell was connected to a gas flow system ( $1\text{ ml min}^{-1}$ ). At first, the sample was pretreated in  $5\%$   $\text{H}_2/\text{Ar}$  at  $200\text{ }^\circ\text{C}$  for 1 h. Then, the cell was flushed with Ar for another 30 min and cooled to reaction temperature ( $160\text{ }^\circ\text{C}$ ) before the following IR measurements. After the collection of background spectra, the reaction gas ( $1\%$   $\text{CO}_2$ ,  $5\%$   $\text{H}_2$ , and  $94\%$  Ar in volume) was continuously introduced into the cell and steady-state spectra were collected after 10 min of reaction at  $160\text{ }^\circ\text{C}$ . As for the  $\text{CO}_2$  reduction under “heating and illumination”, an IR-cut filter was mounted onto the Xe lamp to avoid the interference of IR light. The filtered light ( $<800\text{ nm}$ ,  $0.4\text{ W cm}^{-2}$ ) was illuminated onto the sample through the quartz window and the temperature was also maintained at  $160\text{ }^\circ\text{C}$  with assistant heating. Stead-state spectra were then collected after 10 min of reaction at  $160\text{ }^\circ\text{C}$ .

### 2.5 Localized temperature simulation

Localized temperature simulation was performed using the software (Lumerical, Canada) of *FDTD Solutions* (8.15.736) and *Device-Heat* (5.0.736). The optical absorption data calculated by *FDTD Solutions* was used as a heat input for the *Heat* simulation. The input light was set at  $425\text{ nm}$  (its  $T$  simulation result was close to the average value in the range of solar light), and its light intensity was set at  $1.1\text{ W cm}^{-2}$  to match the real conditions in our experiments. The minimum mesh interval for MF and  $T$  simulations were  $0.08\text{ nm}$  and  $0.01\text{ nm}$ , respectively. The material parameters of Ru are obtained from the Palik data.<sup>16</sup> The optical parameters ( $n$ ,  $k$ ) of the  $\text{CeO}_2$  support were measured using a dual rotating-compensator Mueller matrix ellipsometer (ME-L ellipsometer, Wuhan Eoptics Technology Co., Wuhan, China), and the thermal conductivity of the  $\text{CeO}_2$  support was set as  $7.4\text{ W mK}^{-1}$ .

### 2.6 DFT theoretical calculation

All calculations were performed using the first-principles density of functional theory DFT+U calculations implemented in the Vienna *ab initio* simulation package (VASP)<sup>17,18</sup> with the exchange–correlation functions, which were described by generalized gradient approximation (GGA) with the Perdew–Burke–Ernzerhof (PBE) function.<sup>19</sup> The  $\text{Ce-5s}^25\text{p}^66\text{s}^24\text{f}^15\text{d}^1$ ,  $\text{C-2s}^22\text{p}^2$ ,  $\text{O-2s}^22\text{p}^4$ , and H-1s states were considered as valence states within the projector augmented wave (PAW) method representing the electron–ion interaction with an  $a$  plane wave cutoff of  $450\text{ eV}$ .<sup>15,20,21</sup> To minimize the exchange interactions of the strongly localized Ce 4f electrons, we used the  $5\text{ eV}$  value for  $U$  on the basis of the theoretical tests in the literature.<sup>22</sup>

The  $\text{CeO}_2$  (111) surface was modeled using a  $(3 \times 3)$  supercell with a thickness of 9 atomic layers, and the vacuum thickness being larger than  $20\text{ \AA}$  in the  $\langle 111 \rangle$  direction. During optimization, the energy and force converged to  $10^{-5}\text{ eV}$  per atom and  $0.02\text{ eV \AA}^{-1}$ . A grid of  $3 \times 3 \times 1$  Monkhorst–Pack mesh k-points was used to perform integration in the Brillouin zone.<sup>23</sup>

## 3. Results and discussion

### 3.1 Characterization of the Ru/CeO<sub>2</sub> catalyst

A representative TEM image of the as-prepared  $\text{CeO}_2$  shows that the sample consists of nanoparticles with an average particle size of  $\sim 5\text{ nm}$  (Fig. 3a). The combination of these nanoparticles was found to remain unbroken after continuous ultrasonic dispersion. Moreover, no individual nanoparticles are observed, which indicates that these nanoparticles grew together instead of random agglomeration. High-resolution transmission electron microscopy (HRTEM) analysis shows that the nanoparticles are crystalline and have an identical lattice fringe of  $0.31\text{ nm}$  corresponding to the interplanar spacing of the (111) plane of  $\text{CeO}_2$  (Fig. 3b). Meanwhile, the dislocations of lattice fringes could be observed between the boundaries of neighboring nanoparticles. The HRTEM image of Ru/CeO<sub>2</sub> clearly shows the deposition of fine Ru nanoparticles with an average particle size of  $\sim 2\text{ nm}$  (Fig. 3c and S2†).

The EDS result gives evidence for the existence of Ru (Fig. S3†). In the enlarged HRTEM image of the edging part, the lattice fringe of  $0.21\text{ nm}$  matches well with that of the (002) plane of Ru (Fig. 3d). Fig. 3e shows the XRD patterns of the Ru/CeO<sub>2</sub> sample and the reflection peaks can be indexed to the fluorite structure of  $\text{CeO}_2$  (JCPDS file no. 34-0394). However, no characteristic XRD diffractions are observed for Ru in the Ru/CeO<sub>2</sub> sample, indicative of the small size of Ru particles. For the optical properties revealed by the diffuse reflectance spectra (Fig. 3f), the bare  $\text{CeO}_2$  sample only exhibits obvious absorption in the ultraviolet region. In comparison, the visible-light absorption is greatly enhanced on the Ru/CeO<sub>2</sub> sample. The enhanced light absorption is attributed to the existence of Ru nanoparticles, which capture the light energy through the interband transition of bound electrons.<sup>24,25</sup>

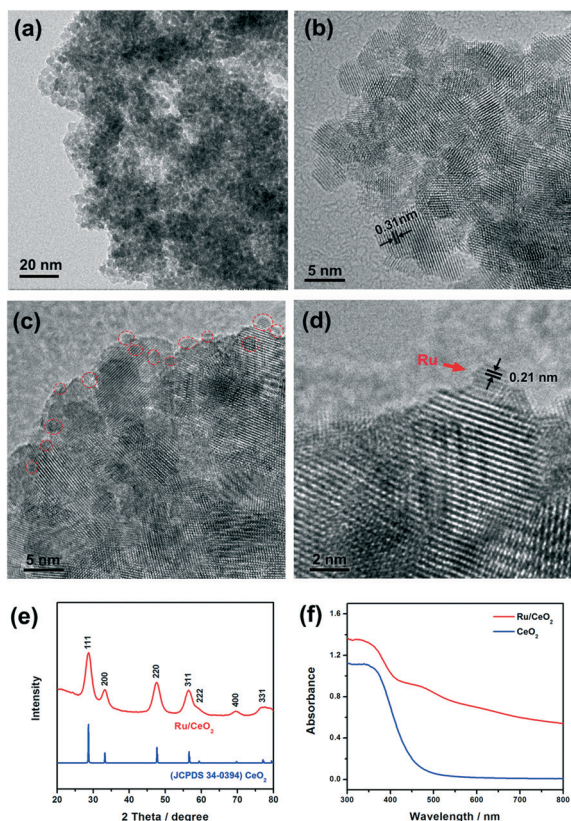


**Fig. 3** (a) TEM image of the  $\text{CeO}_2$  sample. (b) HRTEM image of the  $\text{CeO}_2$  sample. (c) HRTEM image of the  $\text{Ru}/\text{CeO}_2$  sample (the location of Ru nanoparticles are labeled by the red circles). (d) HRTEM image of the edging part of the  $\text{Ru}/\text{CeO}_2$  sample. (e) XRD patterns of the  $\text{Ru}/\text{CeO}_2$  sample. (f) Diffusive reflectance spectra of the  $\text{CeO}_2$  and  $\text{Ru}/\text{CeO}_2$  samples.

XPS analyses were carried out to investigate the surface structure of the as-synthesized  $\text{CeO}_2$  and  $\text{Ru}/\text{CeO}_2$  samples. As illustrated in Fig. 4, six peaks resulting from the  $\text{Ce}^{4+}$  state exist in the spectra of the  $\text{CeO}_2$  sample. Another two peaks (around 884.3 eV and 902.9 eV), which are attributed to the  $3d_{5/2}$  and  $3d_{3/2}$  peaks from the  $\text{Ce}^{3+}$  state ( $u'$  and  $v'$ ),<sup>26,27</sup> could be easily observed in the XPS spectrum of  $\text{CeO}_2$ . However, these two peaks are weakened significantly in the  $\text{Ru}/\text{CeO}_2$ . It is well known that the existence of  $\text{Ce}^{3+}$  in  $\text{CeO}_2$  leads to the generation of oxygen vacancies,<sup>12</sup> which favors the stable anchoring of metal nanoparticles.<sup>28,29</sup> Therefore, the deposition of Ru nanoparticles tends to take place on the  $\text{Ce}^{3+}$  sites. As for the Ru XPS spectra in Fig. S4,<sup>†</sup> the peaks at around 281.6 eV can be attributed to the oxidized Ru species.<sup>14</sup> After  $\text{H}_2$  pretreatment, this peak shifted to a lower binding energy of 280.9 eV, indicating its reduction to  $\text{Ru}^0$  species.<sup>30</sup>

Moreover, the interaction between the Ru and  $\text{CeO}_2$  substrate should be strong, as illustrated by the  $\text{H}_2$ -TPR measurements in Fig. 5. For the  $\text{CeO}_2$  without Ru loading, three peaks at 260, 370 and 450 °C are assigned to the reduction of surface  $\text{CeO}_2$ , while the peak at 810 °C corresponds to the reduction of bulk  $\text{CeO}_2$ . After the Ru deposition on  $\text{CeO}_2$ , the peak intensity at 260 °C was dramatically enhanced, indicating that a large

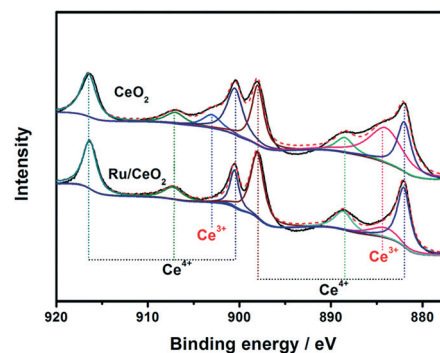


**Fig. 4** XPS analysis of the Ce 3d spectra of the  $\text{CeO}_2$  and  $\text{Ru}/\text{CeO}_2$  samples. Black curves represent the original results while other colored solid lines represent the fitting curves corresponding to that of the specific cerium species. The dashed curves are drawn from the summation of data from the fitting curves.

amount of  $\text{H}_2$  is consumed in the reduction of surface  $\text{CeO}_2$ . This unique phenomenon illustrates the strong interaction between Ru and  $\text{CeO}_2$ , and the dissociated hydrogen on Ru nanoparticles could be transferred efficiently to  $\text{CeO}_2$  for hydrogenation. It is noted that the weak peak at 80 °C was attributed to the reduction of the oxide layer of Ru nanoparticles.<sup>14</sup> Moreover, this peak disappeared in the TPR result of the  $\text{Ru}/\text{CeO}_2$  sample after hydrogen pretreatment at 150 °C (Fig. S5,<sup>†</sup>), indicating that the ruthenium component was reduced after pretreatment. Then, the  $\text{Ru}/\text{CeO}_2$  sample was used as a model catalyst in the following study on  $\text{CO}_2$  hydrogenation.

### 3.2 Contribution of light to $\text{CO}_2$ hydrogenation on $\text{Ru}/\text{CeO}_2$

Under illumination, it is unavoidable that light-induced heating will cause a temperature increase in the catalysts. To figure out if heating was the sole factor in triggering the  $\text{CO}_2$  hydrogenation, the relationship between the illumination power and the resulting temperature was first measured (Fig. S6,<sup>†</sup>), and then the illumination power was adjusted to maintain a certain temperature. In the contrast experiment of “heating”, illumination was cut off and a hotplate was used to achieve the same temperature. Fig. 6a shows the

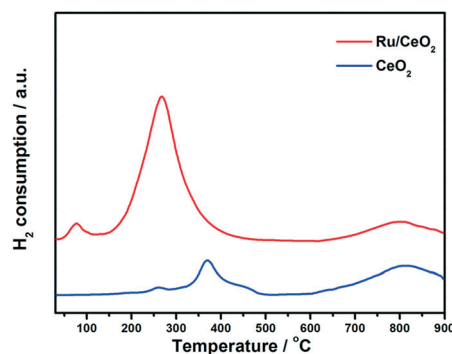


**Fig. 5**  $\text{H}_2$ -TPR profiles of  $\text{CeO}_2$  and  $\text{Ru}/\text{CeO}_2$  catalysts. The peak at 80 °C in  $\text{Ru}/\text{CeO}_2$  resulted from the reduction of the oxide film of Ru nanoparticles.

comparison of CO<sub>2</sub> conversion under two different reaction conditions (“illumination” and “heating” in Fig. 1) for the Ru/CeO<sub>2</sub> and CeO<sub>2</sub> catalysts. Over the temperature range, the CO<sub>2</sub> conversion under illumination is much higher than that under heating.

The CO<sub>2</sub> conversion under illumination reaches 99.9% at 160 °C (corresponding to an illumination power of 1.1 W cm<sup>-2</sup>, Fig. 6a), which is almost 6 times higher than that under heating. A similar positive effect of illumination was also observed on the Ru/CeO<sub>2</sub> catalysts by the use of another reaction gas mixture with low CO<sub>2</sub> concentration (Fig. S7†). To figure out if CeO<sub>2</sub> itself could contribute to the enhanced CO<sub>2</sub> conversion under illumination, comparative experiments were conducted over the CeO<sub>2</sub> sample, and individual CeO<sub>2</sub> exhibited almost negligible activities in both reaction models. Therefore, sole CeO<sub>2</sub> could not bring light-induced enhancement in CO<sub>2</sub> conversion. These primary results show that illumination could significantly facilitate CO<sub>2</sub> reduction on Ru/CeO<sub>2</sub>.

The distribution of products over Ru/CeO<sub>2</sub> is shown in Fig. S8† and the selectivity of methane is nearly 100%. Under these two different reaction models, a much lower concentration (less than 10 ppm) of CO was detected in the products and its molar ratio as compared with methane is near to zero, indicating the selectivity of methane was not affected by the reaction conditions. Moreover, the Ru/CeO<sub>2</sub> catalyst exhibited no decrease in continuous 30 h light-driven reaction (Fig. 6b), while there was 24% degradation in the thermocatalytic process. The reason for the decrease of the CO<sub>2</sub> conversion rate

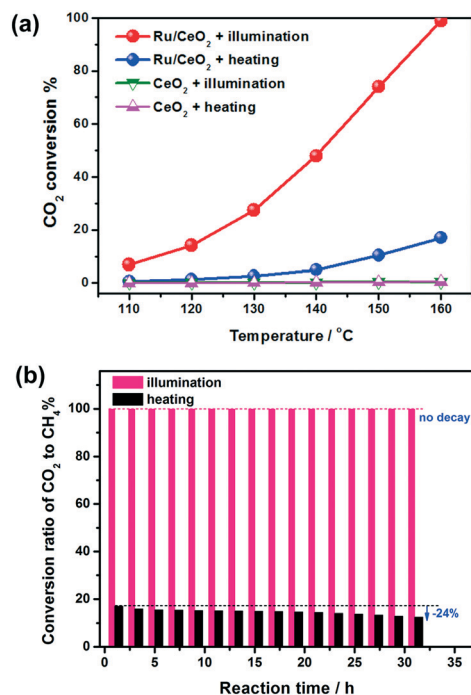


Fig. 6 (a) CO<sub>2</sub> conversion over the Ru/CeO<sub>2</sub> catalyst under the “illumination” or “heating” model. (b) Conversion ratio of CO<sub>2</sub> to CH<sub>4</sub> over the Ru/CeO<sub>2</sub> catalyst under illumination only or heating only during long-time reaction. The illumination power was controlled to reach 160 °C, which is the same as that under heating only.

in the thermal process could be that the intermediate species accumulated gradually and occupied the active sites at this reaction temperature. Under the illumination process, the conversion of intermediate species was efficient and the high activity of the catalyst was well maintained.

The impact of light intensity on the reaction rate of CO<sub>2</sub> hydrogenation was investigated by varying the irradiance power, while other experimental conditions were kept unchanged and the reaction temperature was maintained at 160 °C by assistant heating (model c in Fig. 1). The relative contribution of heat to the reaction rate was calculated by the division of the rate under heating only (160 °C) by the rate under “illumination + heating”. Then the relative contribution of illumination could be determined. With the increase of the illumination power from 0.6 to 1.1 W cm<sup>-2</sup>, the reaction rate increases from 2.1 to 4.9 mmol CH<sub>4</sub> g<sub>cat</sub><sup>-1</sup> h<sup>-1</sup> in a nearly linear relationship (Fig. 7). At the same time, the contribution of light also rises to 83% of the reaction rate at an illumination power of 1.1 W cm<sup>-2</sup>. Since the reaction temperature was strictly controlled to ensure the temperature uniformity, the enhanced activity under illumination mainly originates from the light rather than the thermal effect.

Under illumination, it is probable that there was a difference between the measured temperature and practical temperature on the nanoparticle surface. This factor could be the reason for the superior reaction rate in the light-driven process. In order to verify this speculation, a theoretical model (see detailed introduction in the experimental section) was used to calculate the temperature increase ( $\Delta T$ ) on the Ru nanoparticles and CeO<sub>2</sub> substrate upon illumination. It can be seen in Fig. 8a that there is only a 1–4 K rise of temperature under a laser power of 1.1 W cm<sup>-2</sup>. This means that the difference between the localized temperature and the measured temperature using a thermocouple is too small to account for obvious enhancement in the reaction rate. Therefore, the effect of local heating on nanoparticles could be eliminated, and the enhanced conversion of CO<sub>2</sub> on Ru/CeO<sub>2</sub> under illumination is definitely associated with the light effect.

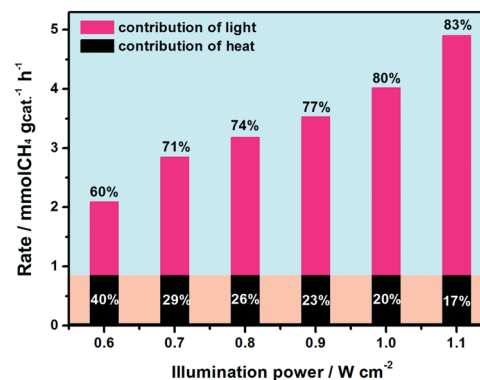


Fig. 7 The contributions of light and heat to the conversion rates under “illumination + heating”. The reaction temperature was maintained at 160 °C by assistant heating.

Then how does the light affect the special activity of Ru/CeO<sub>2</sub> in CO<sub>2</sub> hydrogenation? One possibility is that the light may accelerate a particular key step in the CO<sub>2</sub> hydrogenation process, which is different from that in the thermal process. If so, the apparent activation energy ( $E_a$ ) in these two processes should be different. To check this hypothesis, the value of  $E_a$  for CO<sub>2</sub> methanation was calculated from the Arrhenius plot by using the following equation:  $E_a = -Rd(\ln r)/d(1/T)$  (Fig. 8b). The  $E_a$  for CO<sub>2</sub> methanation under illumination (74.8 kJ mol<sup>-1</sup>) is lower than that under heating (92.2 kJ mol<sup>-1</sup>). The decrease of  $E_a$  indicates that the light irradiation favors the reduction of activation energy, which leads to an increased reaction rate.

### 3.3 *In situ* FTIR characterization of intermediate species and DFT analysis

*In situ* Fourier transform infrared spectroscopy (FTIR) studies were carried out to obtain further insight into the enhanced activity of Ru/CeO<sub>2</sub> under illumination. At first, CO<sub>2</sub> and H<sub>2</sub> were introduced continuously into the cell which is heated at 160 °C, and steady FTIR spectra were obtained after 10 min reaction (Fig. 9). The IR bands at 1544, 1388, 1297, 1217 and 1048 cm<sup>-1</sup> represent different vibrational modes of carbonates<sup>31,32</sup> adsorbed on CeO<sub>2</sub> with reference to the IR information in Fig. S9.† The peak at 1604 cm<sup>-1</sup> is assigned to the antisymmetric OCO vibration of formate-like intermediate species during the conversion of CO<sub>2</sub> to methane.<sup>13,33,34</sup> After comparing this result with the following DFT calculation (discussed later), we believe that the peak at 1604 cm<sup>-1</sup> probably originated from the \*OCOH species.

Then the reaction condition was changed to “heating + illumination” with filtered light (without IR content) to investigate the effect of illumination on the CO<sub>2</sub> hydrogenation. After the spectra became steady again, the intensity of the \*OCOH band decreased significantly while the methane signal at 3016 cm<sup>-1</sup> increased (Fig. 9). It is believed that the formate species are the key intermediates for the production of methane.<sup>14,18</sup> This sharp contrast indicates that illumination may accelerate the conversion of formate intermediates (\*OCOH species) to methane, which leads to a decreased coverage of formate intermediates on the catalyst surface.

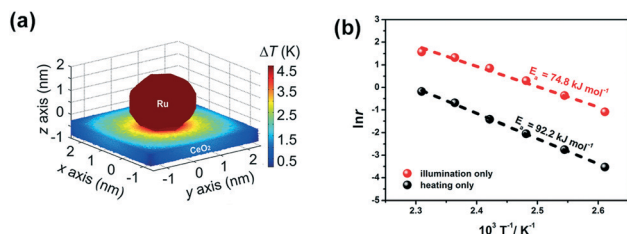


Fig. 8 (a) Model calculation of the temperature enhancement on the Ru/CeO<sub>2</sub> matrix at a fixed laser intensity of 1.1 W cm<sup>-2</sup>. (b) Arrhenius plots of CH<sub>4</sub> formation over Ru/CeO<sub>2</sub> catalysts under illumination only or heating only.

Besides the formate species, the CO band could be observed at 2013 cm<sup>-1</sup> during thermal CO<sub>2</sub> hydrogenation. This should be assigned to the CO produced in the CO<sub>2</sub> hydrogenation and linearly bound to the Ru nanoparticle.<sup>35</sup> There is no obvious change in the intensity of the CO band before and after imposition of illumination, indicating that illumination causes little effect on the CO species. Moreover, no methane was obtained when using CO as the precursor gas, further suggesting that CO is not the intermediate for the formation of methane here. The illumination also accelerated the conversion of carbonates adsorbed on the surface of cerium oxide. Compared with other peaks of carbonates, the intensity of the peak at 1544 cm<sup>-1</sup> (unidentate carbonate) decayed more pronouncedly, indicating that light might promote the transformation of carbonate adsorbed in this configuration.

As mentioned by previous articles on CO<sub>2</sub> hydrogenation utilizing “metal nanoparticles/CeO<sub>2</sub>” catalysts, metal nanoparticles accounted for the dissociation of hydrogen and the CeO<sub>2</sub> substrate was responsible for the adsorption and activation of CO<sub>2</sub>.<sup>12</sup> Here, the ruthenium component of the Ru/CeO<sub>2</sub> catalyst is responsible for hydrogen splitting in the CO<sub>2</sub> hydrogenation process, as indicated by calculation results in Fig. S10.† To further investigate the effect of illumination on the conversion of formate-like intermediates, we performed calculations on cerium oxide to determine possible intermediates and built the potential reaction pathway (Fig. 10a). In the first step of hydrogenation, the formation of \*OCOH (H added to the O atom of \*CO<sub>2</sub>,  $\Delta E = 0.35$  eV) is thermodynamically more favorable than that of \*OCHO (H added to the C atom of \*CO<sub>2</sub>,  $\Delta E = 1.73$  eV). Following the \*OCOH intermediate, a series of hydrogenation steps are conducted to produce methane. Although the total energy expenditure towards conversion of CO<sub>2</sub> to CH<sub>4</sub> is small (0.25 eV), the conversion of \*OCOH to \*OCHOH species is endothermic with the highest reaction energy ( $\Delta E = 0.84$  eV).

Further calculation uncovers the activation energies of the initial three reaction steps (Fig. 10b). It can be seen that the second hydrogenation step is up against an energy barrier of

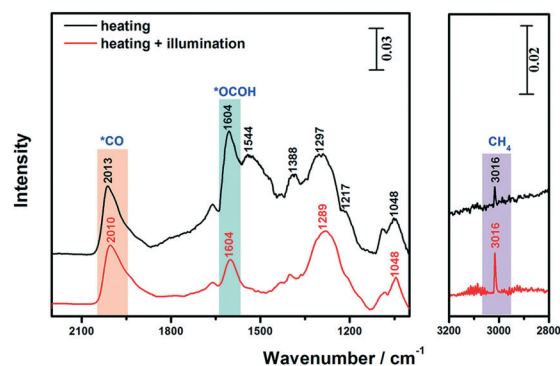
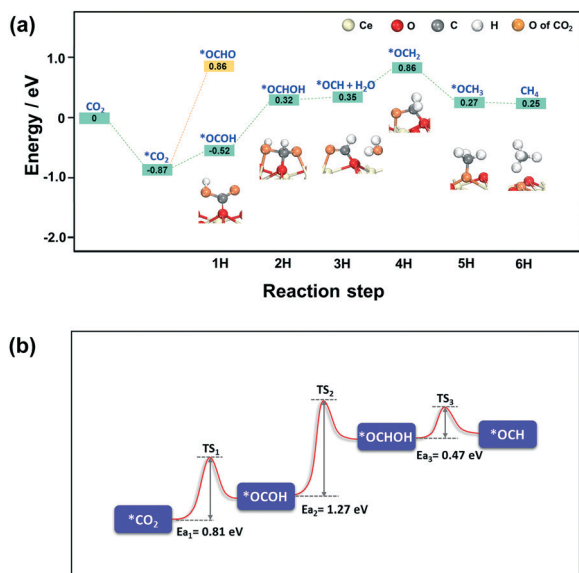


Fig. 9 Steady FTIR spectra recorded over the Ru/CeO<sub>2</sub> catalyst after continuous feed of reaction gas (CO<sub>2</sub> and H<sub>2</sub>) under heating, and then under “heating + illumination” at 160 °C.



**Fig. 10** (a) Potential energy diagrams for the hydrogenation of CO<sub>2</sub> to CH<sub>4</sub> on CeO<sub>2</sub> (111) surfaces. The optimized structures of intermediates are illustrated in the bottom part. (b) Activation energies of the initial three steps listed in (a). TS represents the transition state.

1.27 eV, which is much higher than that of the first or the third hydrogenation step. Therefore, the second hydrogenation step could be rate-determining and a high energy is required to trigger the conversion of \*OCO. This is in good agreement with the results in Fig. 9 indicating that the considerable IR signal from the \*OCO intermediate could be observed during the reaction process. By contrast, there is no characteristic IR band of  $\nu(\text{C-H})$  from \*OCHOH observed at  $\sim 2850\text{ cm}^{-1}$  (Fig. 9), indicating that the hydrogenation of \*OCHOH is not the rate-determining step.

Based on the above analysis, the reason for the high conversion rate of CO<sub>2</sub> under illumination could be that the light can effectively promote the activation of \*OCO species and overcome the energy barrier for its subsequent conversion. In this case, the CeO<sub>2</sub> substrate played a key role in the illumination process due to its special properties in photo-absorbance. An Al<sub>2</sub>O<sub>3</sub> material without photo-absorbance was used as a substrate to support the Ru nanoparticles, and the results showed no obvious difference in CO<sub>2</sub> conversion under “illumination” and “heating” models (Fig. S11†). The contrast experimental results further demonstrate the crucial relationship between the photo-absorbance capability of the CeO<sub>2</sub> substrate and the increase of CO<sub>2</sub> conversion on Ru/CeO<sub>2</sub> under illumination. In the “heating” model, thermo-energy is the only driving force to complete the CO<sub>2</sub> hydrogenation. The CeO<sub>2</sub> substrate provides the active sites for the adsorption of CO<sub>2</sub> while the Ru component contributes to the hydrogen dissociation. In the “illumination” model, the photo-energy adsorbed by CeO<sub>2</sub> may facilitate the activation of intermediates in the rate-determining step of CO<sub>2</sub> hydrogenation. With the cooperation of dissociated hydrogen on Ru, the efficient conversion of these key intermediates finally contributes to the overall conversion of CO<sub>2</sub> to methane. Fur-

ther work will be carried out on the detailed mechanism of photo-induced activation of intermediates on the interface of the substrate. Present results may provide a new understanding on the effect of light on the catalytic process, and this strategy could also be applied to other catalytic processes to realize a reduction in reaction temperature.

## 4. Conclusions

In this study, the light-driven CO<sub>2</sub> hydrogenation was systematically investigated on Ru/CeO<sub>2</sub> catalysts. The results illustrated that the CO<sub>2</sub> hydrogenation under illumination was more efficient than that under thermal heating. At a low temperature of 160 °C, the corresponding reaction rate ( $4.9\text{ mmol g}_{\text{cat}}^{-1}\text{ h}^{-1}$ ) is about 6 times higher than that performed under heating only ( $0.83\text{ mmol g}_{\text{cat}}^{-1}\text{ h}^{-1}$ ). Moreover, the activities of the sample exhibit no decrease in continuous 30 h light-driven reaction, while there is 24% degradation in the thermocatalytic process. Further analysis reveals that the enhanced activity mainly results from the light rather than the thermal effect. The apparent activation energy for CO<sub>2</sub> methanation under illumination ( $74.8\text{ kJ mol}^{-1}$ ) is found to be lower than that under heating ( $92.2\text{ kJ mol}^{-1}$ ), indicating that light irradiation favors the decrease of activation energy. As revealed by the *in situ* IR analysis and theoretical calculation, the illumination may accelerate the conversion of adsorbed intermediate species, which leads to an increased yield rate. We anticipate that this work may provide deep understanding of the CO<sub>2</sub> hydrogenation process under illumination, and this strategy may be extended to other hydrogenation processes.

## Conflicts of interest

There are no conflicts to declare.

## Acknowledgements

This work was supported by the National Science Foundation of China (Grant 21777050), the National Key Research and Development Program of China (Grant 2016YFA0203002), and the National Natural Science Funds for Distinguished Young Scholars (21425728).

## References

- 1 M. D. Porosoff, B. Yan and J. G. Chen, *Energy Environ. Sci.*, 2016, **9**, 62–73.
- 2 W.-H. Wang, Y. Himeda, J. T. Muckerman, G. F. Manbeck and E. Fujita, *Chem. Rev.*, 2015, **115**, 12936–12973.
- 3 Y. Yan, Y. Dai, H. He, Y. Yu and Y. Yang, *Appl. Catal., B*, 2016, **196**, 108–116.
- 4 C. Janke, M. S. Duyar, M. Hoskins and R. Farrauto, *Appl. Catal., B*, 2014, **152**, 184–191.
- 5 Z.-W. Zhao, X. Zhou, Y.-N. Liu, C.-C. Shen, C.-Z. Yuan, Y.-F. Jiang, S.-J. Zhao, L.-B. Ma, T.-Y. Cheang and A.-W. Xu, *Catal. Sci. Technol.*, 2018, **8**, 3160–3165.

- 6 H. C. Wu, Y. C. Chang, J. H. Wu, J. H. Lin, I. K. Lin and C. S. Chen, *Catal. Sci. Technol.*, 2015, 5, 4154–4163.
- 7 X. Meng, T. Wang, L. Liu, S. Ouyang, P. Li, H. Hu, T. Kako, H. Iwai, A. Tanaka and J. Ye, *Angew. Chem.*, 2014, 126, 11662–11666.
- 8 L. Lin, K. Wang, K. Yang, X. Chen, X. Fu and W. Dai, *Appl. Catal., B*, 2017, 204, 440–455.
- 9 Y. Ma, Y. Li, M. Mao, J. Hou, M. Zeng and X. Zhao, *J. Mater. Chem. A*, 2015, 3, 5509–5516.
- 10 Y. Zheng, W. Wang, D. Jiang, L. Zhang, X. Li and Z. Wang, *J. Mater. Chem. A*, 2016, 4, 105–112.
- 11 M. A. A. Aziz, A. A. Jalil, S. Triwahyono and A. Ahmad, *Green Chem.*, 2015, 17, 2647–2663.
- 12 F. Wang, M. Wei, D. G. Evans and X. Duan, *J. Mater. Chem. A*, 2016, 4, 5773–5783.
- 13 F. Wang, S. He, H. Chen, B. Wang, L. Zheng, M. Wei, D. G. Evans and X. Duan, *J. Am. Chem. Soc.*, 2016, 138, 6298–6305.
- 14 F. Wang, C. Li, X. Zhang, M. Wei, D. G. Evans and X. Duan, *J. Catal.*, 2015, 329, 177–186.
- 15 S. Hilaire, L. Luo, F. Rechberger, F. Krumeich and M. Niederberger, *Z. Anorg. Allg. Chem.*, 2014, 640, 733–737.
- 16 E. D. Palik, *Handbook of optical constants of solids*, Academic press, U.S.A., 1st edn, 1997.
- 17 J. P. Perdew, K. Burke and M. Ernzerhof, *Phys. Rev. Lett.*, 1996, 77, 3865.
- 18 G. Kresse and D. Joubert, *Phys. Rev. B: Condens. Matter Mater. Phys.*, 1999, 59, 1758–1775.
- 19 G. Kresse and J. Furthmüller, *Phys. Rev. B: Condens. Matter Mater. Phys.*, 1996, 54, 11169–11186.
- 20 P. E. Blöchl, *Phys. Rev. B: Condens. Matter Mater. Phys.*, 1994, 50, 17953–17979.
- 21 X. Lu, W. Wang, S. Wei, C. Guo, Y. Shao, M. Zhang, Z. Deng, H. Zhu and W. Guo, *RSC Adv.*, 2015, 5, 97528–97535.
- 22 M. Nolan, S. C. Parker and G. W. Watson, *Phys. Chem. Chem. Phys.*, 2006, 8, 216–218.
- 23 M. V. Ganduglia-Pirovano, J. L. F. Da Silva and J. Sauer, *Phys. Rev. Lett.*, 2009, 102, 026101.
- 24 X.-N. Guo, Z.-F. Jiao, G.-Q. Jin and X.-Y. Guo, *ACS Catal.*, 2015, 5, 3836–3840.
- 25 S. Sarina, H.-Y. Zhu, Q. Xiao, E. Jaatinen, J. Jia, Y. Huang, Z. Zheng and H. Wu, *Angew. Chem.*, 2014, 126, 2979–2984.
- 26 C. He, X. Liu, J. Shi, C. Ma, H. Pan and G. Li, *J. Colloid Interface Sci.*, 2015, 454, 216–225.
- 27 D. Jiang, W. Wang, Y. Zheng and L. Zhang, *Appl. Catal., B*, 2016, 191, 86–93.
- 28 J. A. Farmer and C. T. Campbell, *Science*, 2010, 329, 933–936.
- 29 M. Baron, O. Bondarchuk, D. Stacchiola, S. Shaikhutdinov and H. J. Freund, *J. Phys. Chem. C*, 2009, 113, 6042–6049.
- 30 J. Tan, J. Cui, X. Cui, T. Deng, X. Li, Y. Zhu and Y. Li, *ACS Catal.*, 2015, 5, 7379–7384.
- 31 G. Marbán, I. López and T. Valdés-Solís, *Appl. Catal., A*, 2009, 361, 160–169.
- 32 O. Pozdnyakova, D. Teschner, A. Wootsch, J. Kröhnert, B. Steinhauer, H. Sauer, L. Toth, F. C. Jentoft, A. Knop-Gericke, Z. Paál and R. Schlögl, *J. Catal.*, 2006, 237, 1–16.
- 33 X. Wang, H. Shi, J. H. Kwak and J. Szanyi, *ACS Catal.*, 2015, 5, 6337–6349.
- 34 A. Haghofer, D. Ferri, K. Föttinger and G. Rupprechter, *ACS Catal.*, 2012, 2, 2305–2315.
- 35 M. R. Prairie, A. Renken, J. G. Highfield, K. Ravindranathan Thampi and M. Grätzel, *J. Catal.*, 1991, 129, 130–144.

## Supplementary information

### Efficient light-driven CO<sub>2</sub> hydrogenation on Ru/CeO<sub>2</sub> catalysts

Fengjiao Quan<sup>a</sup>, Guangming Zhan<sup>a</sup>, Chengliang Mao<sup>a</sup>, Zhihui Ai<sup>a</sup>, Falong Jia<sup>a,\*</sup>, Lizhi Zhang<sup>a</sup>, Honggang Gu<sup>b</sup> and Shiyuan Liu<sup>b</sup>

<sup>a</sup> Key Laboratory of Pesticide & Chemical Biology of Ministry of Education, Institute of Environmental Chemistry, College of Chemistry, Central China Normal University, Wuhan 430079, P. R. China

<sup>b</sup>State Key Laboratory of Digital Manufacturing Equipment and Technology, Huazhong University of Science and Technology, Wuhan 430074, China

\*Corresponding Author. E-mail: [fljia@mail.ccnu.edu.cn](mailto:fljia@mail.ccnu.edu.cn) Tel/Fax: (86)-27-67867953

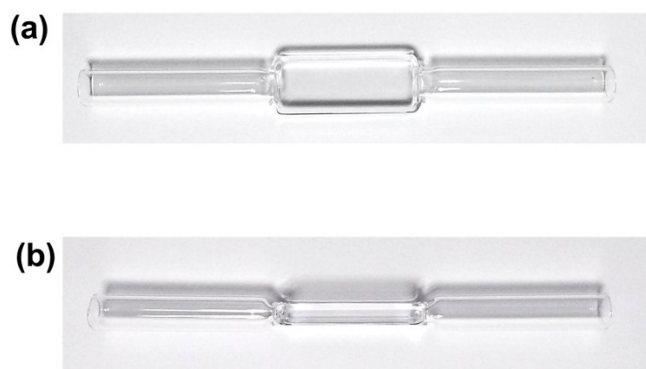
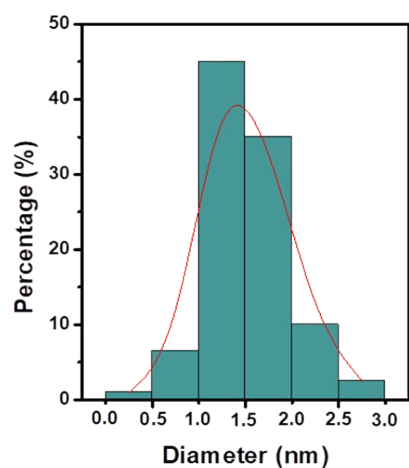


**Fig. S1** Photo images of the flow cell from the top view (a) and side view (b)

As for the loading of catalyst powder, quartz wool was used to block one side of the cuboid cavity, and catalyst powder was then added inside. After that, another side of the cuboid cavity was also blocked with quartz wool. The flow cell was then gently knocked until the catalyst powder vibrated to a uniform spreading.



$$\begin{aligned}\bar{x} &= 0.25*0.01+0.75*0.065+1.25*0.45 \\ &\quad +1.75*0.35+2.25*0.1+2.75*0.025 \\ &= 1.52\end{aligned}$$

$$\begin{aligned}s^2 &= 1/200 [(0.25-1.52)^2*0.01+(0.75-1.52)^2*0.065+(1.25-1.52)^2*0.45 \\ &\quad +(1.75-1.52)^2*0.35+(2.25-1.52)^2*0.1+(2.75-1.52)^2*0.025] \\ &= 0.001\end{aligned}$$

**Fig. S2** The distribution of diameters of Ru nanoparticles and the calculation of average size.

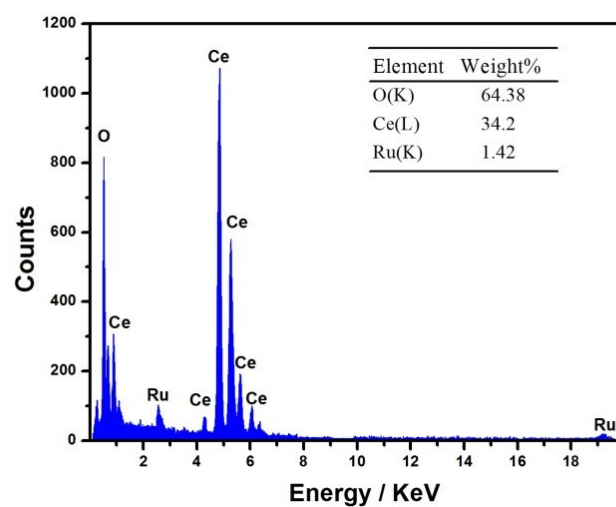


**Fig. S3** EDS spectrum of Ru/CeO<sub>2</sub> sample.

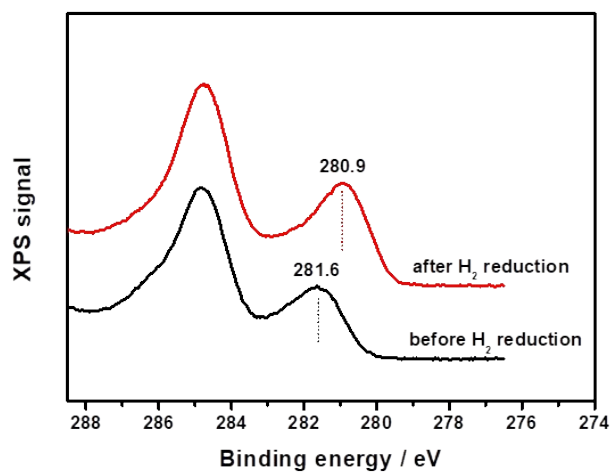


**Fig. S4** XPS analysis of Ru species of Ru/CeO<sub>2</sub> samples before and after H<sub>2</sub> reduction. The peaks at 284.8 eV are attributed to C 1s species arising from adventitious hydrocarbons.

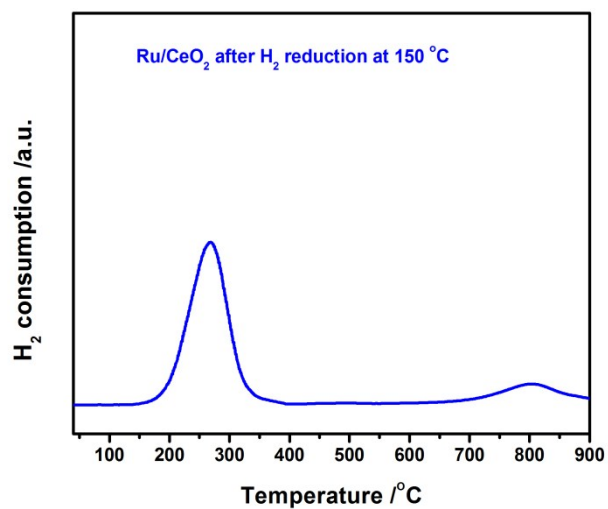


**Fig. S5** H<sub>2</sub>-TPR profiles of Ru/CeO<sub>2</sub> catalysts after hydrogen pretreatment at 150 °C for 1 h.

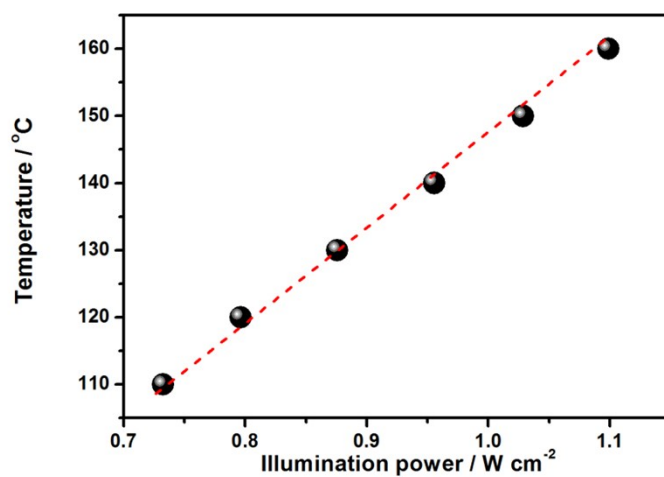


**Fig. S6** The relationship between illumination power and the resulted temperatures on the catalyst.

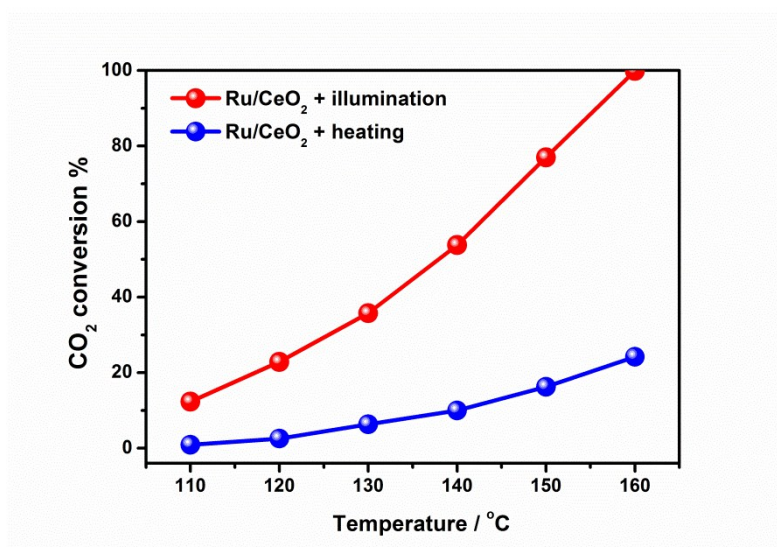


**Fig. S7** CO<sub>2</sub> conversion over Ru/CeO<sub>2</sub> catalyst under “illumination” or “heating” model by the use of another reaction gas mixture (1% CO<sub>2</sub>, 5% H<sub>2</sub>, and 94% Ar in volume).

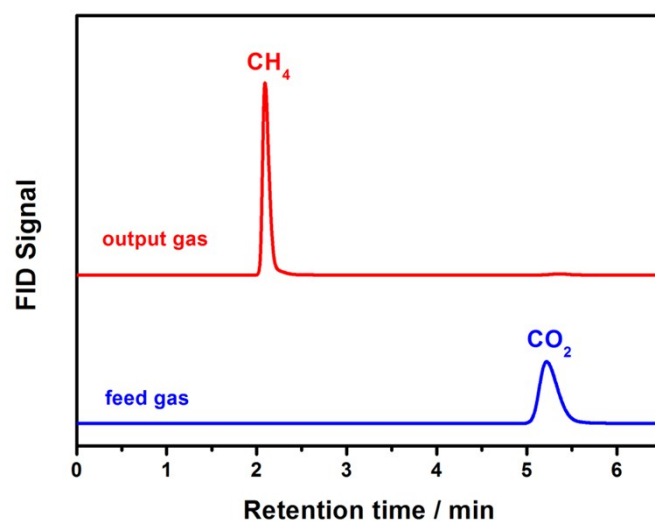


**Fig. S8** Typical GC spectra of the feed gas and output gas obtained over Ru/CeO<sub>2</sub> catalyst under illumination only (1.1 W cm<sup>-2</sup>).

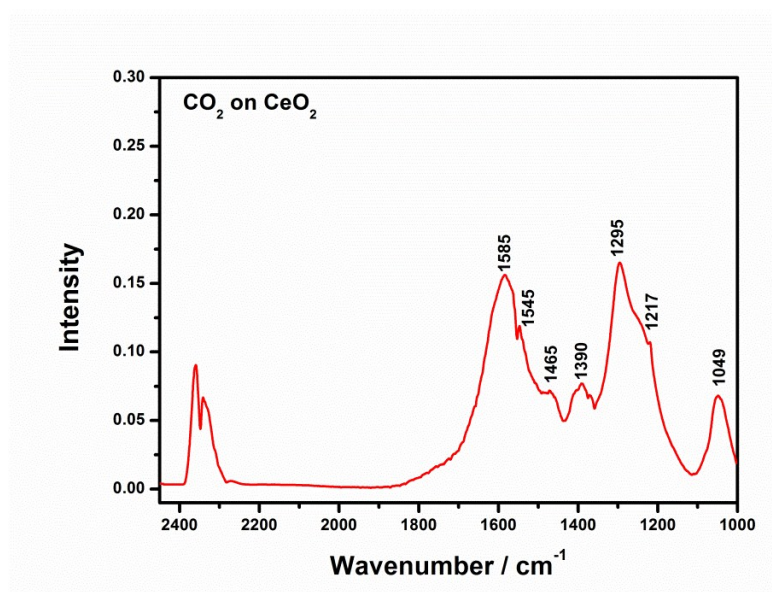


**Fig. S9** FTIR spectra recorded at 160 °C over the CeO<sub>2</sub> catalyst after injection of 0.1 ml pure CO<sub>2</sub> gas into the cell filled with Ar. The IR peaks at 2340 ~ 2360 cm<sup>-1</sup> are assigned to the signals from the gas-phase CO<sub>2</sub>. And other peaks (peak locations are listed on the top of peaks) correspond to the adsorbed CO<sub>2</sub> species on the surface of CeO<sub>2</sub>.

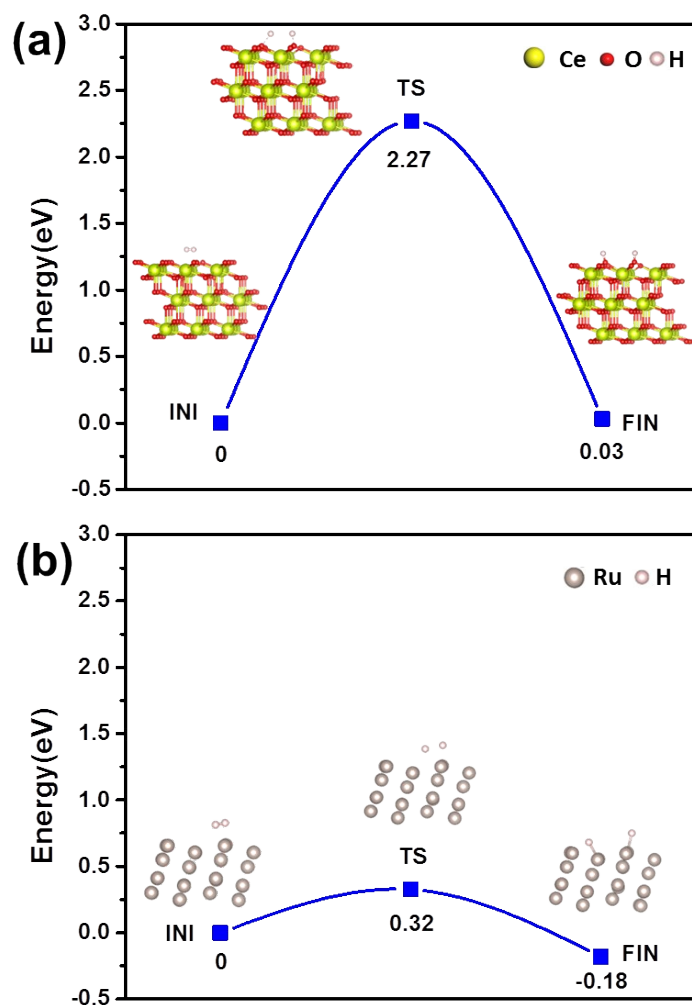


**Fig. S10** Activation energies of hydrogen splitting on the surface of CeO<sub>2</sub> (a) and Ru (b)

The calculated results in Fig. S9 show that the hydrogen splitting on the surface of cerium oxide needs to overcome energy barrier of 2.27 eV, which is much higher than that on the surface of ruthenium (0.32 eV). This sharp contrast indicates that hydrogen molecules tend to be dissociated on ruthenium. Therefore, the ruthenium component of Ru/CeO<sub>2</sub> catalyst is responsible for hydrogen splitting in CO<sub>2</sub> hydrogenation process.

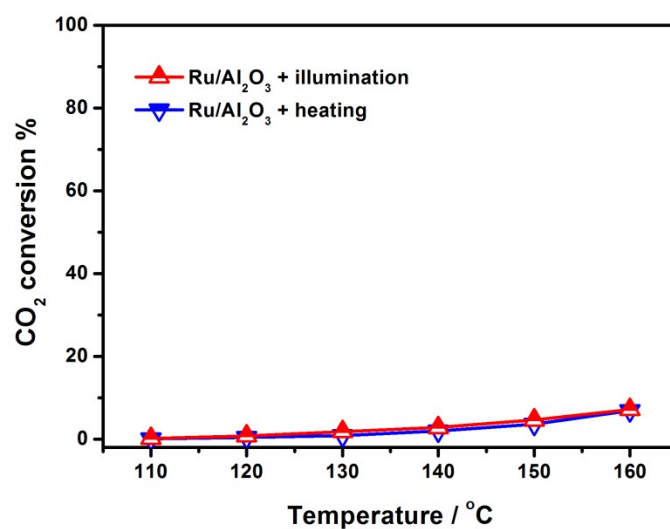


**Fig. S11** CO<sub>2</sub> conversion over Ru/Al<sub>2</sub>O<sub>3</sub> catalyst under “illumination” or “heating” model. In the synthesis procedure of Ru/Al<sub>2</sub>O<sub>3</sub> catalyst, the loading of Ru nanocrystals was same as that of Ru/CeO<sub>2</sub> while commercial Al<sub>2</sub>O<sub>3</sub> nanoparticles (Alfa Aesar, ~20 nm) were used as support material.